

Quantum-interference effects in the $o^1\Pi_u(v=1) \sim b^1\Pi_u(v=9)$ Rydberg–valence complex of molecular nitrogen

M. O. VIEITEZ*†‡, T. I. IVANOV†, J. P. SPRENGERS†, C. A. de LANGE†,
W. UBACHS†, B. R. LEWIS§ and G. STARK¶

†Laser Centre, Vrije Universiteit, De Boelelaan 1081, 1081 HV Amsterdam, The Netherlands

‡AlbaNova Research Centre, Royal Institute of Technology, Stockholm, Sweden

§Research School of Physical Sciences and Engineering,

The Australian National University, Canberra, ACT 0200, Australia

¶Department of Physics, Wellesley College, Wellesley, MA 02481, USA

(Received 19 January 2007; in final form 9 February 2007)

Two distinct high-resolution experimental techniques, 1 XUV + 1' UV laser-based ionization spectroscopy and synchrotron-based XUV photoabsorption spectroscopy, have been used to study the $o^1\Pi_u(v=1) \sim b^1\Pi_u(v=9)$ Rydberg–valence complex of $^{14}\text{N}_2$, providing new and detailed information on the perturbed rotational structures, oscillator strengths, and predissociation linewidths. Ionization spectra probing the $b'^1\Sigma_u^+(v=6)$ state of $^{14}\text{N}_2$, which crosses $o^1\Pi_u(v=1)$ between $J=24$ and $J=25$, and the $o^1\Pi_u(v=1)$, $b^1\Pi_u(v=9)$, and $b'^1\Sigma_u^+(v=6)$ states of $^{14}\text{N}^{15}\text{N}$, have also been recorded. In the case of $^{14}\text{N}_2$, rotational and deperturbation analyses correct previous misassignments for the low- J levels of $o(v=1)$ and $b(v=9)$. In addition, a two-level quantum-mechanical interference effect has been found between the $o\text{-X}(1, 0)$ and $b\text{-X}(9, 0)$ transition amplitudes which is totally destructive for the lower-energy levels just above the level crossing, making it impossible to observe transitions to $b(v=9, J=6)$. A similar interference effect is found to affect the $o(v=1)$ and $b(v=9)$ predissociation linewidths, but, in this case, a small non-interfering component of the $b(v=9)$ linewidth is indicated, attributed to an additional spin–orbit predissociation by the repulsive $3^3\Sigma_u^+$ state.

Keywords: Predissociation; Perturbation; Diatomic molecules; Extreme ultraviolet; Laser spectroscopy

1. Introduction

The dipole-allowed absorption spectrum of molecular nitrogen in the extreme ultraviolet (XUV) wavelength region was initially thought to consist of a multitude of electronic band structures, until the true nature of the excited states was unravelled [1–3]. The apparent complexity of the XUV spectrum is a result of Rydberg–valence mixing between a limited number of singlet *ungerade* states lying at excitation energies just above $100\,000\text{ cm}^{-1}$. There are two valence states involved, one of $^1\Sigma_u^+$ and one of $^1\Pi_u$ symmetry (referred to as the $b'^1\Sigma_u^+$ and $b^1\Pi_u$ states), and there exist singlet Rydberg series converging on the first $X^2\Sigma_g^+$ ionization

limit in the N_2^+ ion (the $np\sigma_u c'_{n+1}^1\Sigma_u^+$ and $np\pi_u c_n^1\Pi_u$ series; principal quantum number $n \geq 3$) and the $ns\sigma_g o_n^1\Pi_u$ series converging on the $A^2\Pi_u$ ionization limit. The vibrational numbering in the $o_3^1\Pi_u$ state, of relevance to the present study, was determined by Ogawa *et al.* [4]. In the seminal paper by Stahel *et al.* [5], a model of Rydberg–valence interactions was presented that provides a quantitative explanation for the energy-level perturbations, the seemingly erratic behaviour of the rotational constants, and the observed pattern of band intensities which deviate strongly from Franck–Condon-factor predictions. A comprehensive *ab initio* study by Spelsberg and Meyer [6] later confirmed the main conclusions of the Stahel *et al.* [5] model. In addition to these homogeneous perturbations in which states of like symmetry are coupled, the effects of heterogeneous perturbations, i.e. coupling between states of $^1\Pi_u$ and $^1\Sigma_u^+$ symmetry, were also included in

*Corresponding author. Email: ofelia@few.vu.nl

subsequent analyses [7], thereby improving the quantitative agreement between theory and experiment. Recently, the inclusion of spin-orbit interactions between the $^1\Pi_u$ and $^3\Pi_u$ states in a coupled-channel model of the Rydberg-valence interactions has allowed the complex isotopic pattern of predissociation in the lower vibrational levels of the $^1\Pi_u$ states to be explained [8], including rotational effects [9].

In addition to the comprehensive theoretical studies describing the overall excited-state structure for dipole-allowed transitions in N_2 [5, 6], several semi-empirical local-perturbation analyses have been performed which focus on particular level crossings. Yoshino *et al.* [10] examined a number of such local perturbations, most of which had one of the $o_3\ ^1\Pi_u(v)$ or $o_4\ ^1\Pi_u(v)$ Rydberg states as a perturbation partner. Yoshino and Freeman [11] treated a multi-level local perturbation involving the Rydberg states $c'_5\ ^1\Sigma_u^+(v=0)$ and $c_5\ ^1\Pi_u(v=0)$ interacting with a number of valence states of $^1\Pi_u$ and $^1\Sigma_u^+$ symmetry. A well-known perturbation, observed as a pronounced feature in N_2 spectra involving the $c'_4\ ^1\Sigma_u^+(v=0)$ and $b'\ ^1\Sigma_u^+(v=1)$ levels, was analysed by Yoshino and Tanaka, based on classical spectroscopic data [12], and later by Levelt and Ubachs, based on XUV-laser data [13]. In the $^{15}N_2$ isotopomer, several local perturbation studies have also been performed, e.g. for the $o\ ^1\Pi_u(v=0) \sim b'\ ^1\Sigma_u^+(v=3)$ crossing [14]. (In the $o_n\ ^1\Pi_u(v)$ series, the subscripts is commonly dropped from the state designation for $n=3$.) Due to differing isotopic shifts in the Rydberg and the valence states, the accidental perturbations occur at different locations in the rovibronic structure of the three natural isotopomers of N_2 .

In this study, the $o\ ^1\Pi_u(v=1) \sim b\ ^1\Pi_u(v=9)$ Rydberg-valence complex of $^{14}N_2$ is examined using two different experimental techniques, providing new and detailed information on the perturbed rotational structures, oscillator strengths, and predissociation linewidths. Rotational and deperturbation analyses are performed which correct previous misassignments [10] for transitions to the low- J levels of $o(v=1)$ and $b(v=9)$, and elucidate the quantum-interference effects occurring in oscillator strength, between these two electric-dipole-allowed transitions, and in linewidth, between these two predissociated levels.

In addition to recording the $b-X(9, 0)$ and $o-X(1, 0)$ bands for the main $^{14}N_2$ isotopomer, these bands were also investigated for $^{14}N^{15}N$ and a rotational analysis performed. In the case of the mixed $^{14}N^{15}N$ isotopomer, the rotational structure of each transition is unperturbed due to differing isotopic shifts. Since, for high J , the homogeneous perturbation complex of the two $^1\Pi_u$ states undergoes a heterogeneous interaction with the

$b'\ ^1\Sigma_u^+(v=6)$ state, as already noticed in $^{14}N_2$ by Yoshino *et al.* [10], the $b'(v=6)$ level is also included in the present study for both $^{14}N_2$ and $^{14}N^{15}N$.

Christian Jungen has made significant contributions to the understanding of the excited states of N_2 . In 1990, Huber and Jungen reported a high-resolution jet absorption study of N_2 in the region near 80 nm [15], unravelling the Rydberg structure and following the vibrational sequence of the $b'\ ^1\Sigma_u^+$ state even beyond the ionization energy. In a subsequent study [16], he was part of a team investigating the *nf*-Rydberg series in the last 6000 cm^{-1} below the ionization energy, based on high-resolution spectra of $^{14}N_2$ and $^{15}N_2$ recorded with the 10.6 m spectrograph at Ottawa and at the Photon Factory synchrotron facility in Tsukuba. Finally, this led to the development of a comprehensive multichannel quantum-defect analysis of the near-threshold spectrum of N_2 [17]. It is with great pleasure that we dedicate our present work to Dr Jungen.

2. Experiments

Two distinct experimental techniques were employed in this work to study the interaction between the $b(v=9)$ and $o(v=1)$ levels of N_2 . First, very-high-resolution laser-based ionization spectroscopy was used to determine the energy perturbations. Second, high-resolution synchrotron-based quantitative photoabsorption spectroscopy was used, primarily to study quantum-interference effects in the corresponding oscillator strengths.

Laser-based $1\text{ XUV} + 1'\text{ UV}$ two-photon ionization spectroscopy was employed to study the excitation spectrum of N_2 , initially in the range $\lambda = 92.9\text{--}93.5\text{ nm}$. Details of the experimental method, including a description of the lasers, vacuum setup, molecular beam configuration, time-of-flight (TOF) detection scheme and calibration procedures, have been given previously [14]. Two different laser systems were used, a pulsed dye laser (PDL)-based source, delivering an XUV bandwidth of $\sim 0.3\text{ cm}^{-1}$ full-width at half-maximum (FWHM), and a pulsed dye amplifier (PDA)-based source, delivering an XUV bandwidth of $\sim 0.01\text{ cm}^{-1}$ FWHM. The wavelength range was later extended to $\lambda = 92.59\text{--}92.87\text{ nm}$, to also cover excitation of the $b'\ ^1\Sigma_u^+(v=6)$ state, which was investigated under similar molecular-beam conditions using the PDL-based source. The PDL-based system and its application to the spectroscopy of N_2 has been described in [14, 18]. Briefly, the sixth harmonic of a pulsed dye laser was employed, calibrated against the reference standard provided by the Doppler-broadened linear absorption

spectrum of molecular iodine [19]. The absolute wave-number uncertainty in the XUV for this system is $\pm 0.1 \text{ cm}^{-1}$ for fully resolved lines. The PDA-based system was used in a frequency-mixing scheme: $\omega_{\text{XUV}} = 3(\omega_{\text{PDA}} + \omega_{532})$, where ω_{532} is the frequency-doubled output of an injection-seeded Nd:YAG laser. It has been documented previously how this frequency-mixing scheme produces a bandwidth of $\sim 0.01 \text{ cm}^{-1}$ FWHM in the XUV [20, 21]. The efficiency for XUV production with this mixing scheme is much lower than for the PDL-based system, and signal levels decrease accordingly. Even though the molecular-beam densities were increased to compensate, this scheme could only be used for calibration (and linewidth measurements) of a few low- J'' lines. In view of the lifetime broadening encountered in the $b(v=9)$ and $o(v=1)$ levels of $^{14}\text{N}_2$ (see also [22]), the absolute accuracy of the corresponding energy calibration was limited to $\sim 0.05 \text{ cm}^{-1}$. The two-photon-ionization TOF experiment has some characteristics that were favourably employed in the present study. Mass separation can be combined with laser excitation to separate the contributions to the spectrum of the main $^{14}\text{N}_2$ isotopomer from those of the mixed $^{14}\text{N}^{15}\text{N}$ species. Even in the case of natural nitrogen, which contains only 0.74% $^{14}\text{N}^{15}\text{N}$, resolved isotopic lines at the bandheads of the $o(v=1)$, $b(v=9)$ – $X(v''=0)$ systems could be observed. However, in a later stage of the experiments, isotopically enriched $^{14}\text{N}^{15}\text{N}$ gas became available, yielding better quality spectra for the b – $X(9,0)$, o – $X(1,0)$, and b' – $X(6,0)$ transitions that were used in the final analysis. Furthermore, by changing the relative delay between the N_2 pulsed-valve trigger and the laser pulse, as well as varying the nozzle-skimmer distance, the rotational temperature in the molecular beam could be selected to measure independent spectra of cold (10–20 K) and warm (up to 180 K) samples. These options helped greatly in the assignment of the spectral lines.

Photoabsorption spectroscopy on the $o(v=1)$, $b(v=9)$ – $X(v''=0)$ systems of $^{14}\text{N}_2$ was performed at the 2.5 GeV storage ring of the Photon Factory, a synchrotron radiation facility at the High Energy Accelerator Research Organization in Tsukuba, Japan. Details of the experimental procedure can be found in Stark *et al.* [23]. Briefly, a 6.65 m spectrometer with a 1200 grooves per mm grating (blazed at 550 nm and used in the sixth order) provided an instrumental resolving power of $\sim 150\,000$, equivalent to a resolution of $\sim 0.7 \text{ cm}^{-1}$ FWHM. The spectrometer tank, at a temperature of 295 K, served as an absorption cell with a path length of 12.51 m. A flowing gas configuration was used: N_2 of normal isotopic composition entered the spectrometer tank through a needle valve and

was continuously pumped by a 1500 s^{-1} turbomolecular pump. Absorption spectra were recorded at tank pressures ranging from 1.8×10^{-5} Torr to 7.5×10^{-5} Torr, corresponding to N_2 column densities ranging from $7.4 \times 10^{14} \text{ cm}^{-2}$ to $3.1 \times 10^{15} \text{ cm}^{-2}$. The 92.88–93.14 nm spectral region was scanned, in three overlapping portions, at a speed of $0.005 \text{ nm min}^{-1}$. A signal integration time of about 1 s resulted in one data point for each $8.7 \times 10^{-5} \text{ nm}$ interval of the spectrum. Signal rates from the detector, a windowless solar-blind photomultiplier tube with a CsI-coated photocathode, were about $50\,000 \text{ s}^{-1}$ for the background continuum; the detector dark count rate was less than 2 s^{-1} . A signal-to-noise ratio of about 250 was typically achieved for the continuum level. The experimental absorption spectra were converted into photoabsorption cross sections through application of the Beer–Lambert law. Non-statistical uncertainties in the experimental cross sections are estimated to be $\sim 10\%$, with contributions from uncertainties in the N_2 column density, variations in the signal background, and scattered light.

3. Results and discussion

3.1. Energies

Using the PDL-based XUV source, rotationally resolved spectra of the $b^1\Pi_u$ – $X^1\Sigma_g^+(9,0)$ and $o^1\Pi_u$ – $X^1\Sigma_g^+(1,0)$ bands in $^{14}\text{N}_2$ were recorded for mass 28 in the TOF spectrum at low and high rotational temperatures, achieved by varying the timing of the N_2 supersonic beam. In figure 1, the two spectra are compared and line assignments shown. High-rotational-temperature laser-excitation spectra were also recorded for $^{14}\text{N}^{15}\text{N}$ using a molecular beam of isotopically enriched nitrogen. Figure 2 shows such a recording, displaying lines from the $b^1\Pi_u$ – $X^1\Sigma_g^+(9,0)$ and $o^1\Pi_u$ – $X^1\Sigma_g^+(1,0)$ bands in $^{14}\text{N}^{15}\text{N}$.

Using the narrower-bandwidth frequency-mixing PDA-based XUV source, spectra of the b – $X(9,0)$ and o – $X(1,0)$ bands in $^{14}\text{N}_2$ were recorded for some low-rotational lines. Recordings of the $Q(2)$ line from the b – $X(9,0)$ band and the $Q(1)$ line from the o – $X(1,0)$ band in $^{14}\text{N}_2$, obtained with this source, are shown in figure 3. Signal levels for the transition to the broader $b(v=9, J=2)$ level are low because of the competition between predissociation and ionization in the $1 + 1'$ two-photon ionization detection scheme and the rather low XUV and UV intensity levels available with the frequency-mixing scheme employed. Analysis of the linewidths and discussion of the predissociation phenomena in the excited states are deferred

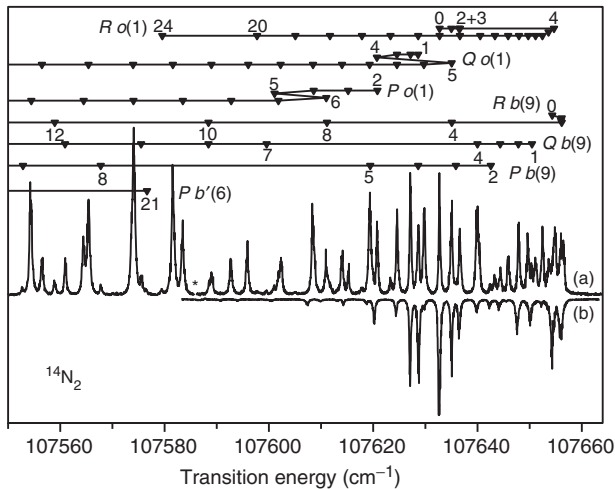


Figure 1. 1 XUV + $1'$ UV ionization spectra and line assignments for the $b^1\Pi_u-X^1\Sigma_g^+(9,0)$ and $o^1\Pi_u-X^1\Sigma_g^+(1,0)$ bands of $^{14}\text{N}_2$ in high (spectrum a) and in low (spectrum b) rotational-temperature molecular beams, recorded using the PDL-based XUV source. Note that severe blending occurs in the spectrum and several weak lines are not identified. In the region in spectrum (a) marked with an asterisk, two separate scans are joined and intensities of the two scans should not be compared.

to section 3.3. Transition energies and line assignments for the $o(v=1)$ and $b(v=9)$ levels (see below) are presented in tables 1 and 2, for $^{14}\text{N}_2$, and in tables 3 and 4, for $^{14}\text{N}^{15}\text{N}$.

An excitation spectrum for the $b^1\Sigma_u^+-X^1\Sigma_g^+(6,0)$ band of $^{14}\text{N}_2$, which lies just above the overlapped $b-X(9,0)$ and $o-X(1,0)$ bands, is shown in figure 4. Assignment of the lines in this $^1\Sigma_u^+-^1\Sigma_g^+$ band, containing only P and R branches, is straightforward, but the rotational constants for the ground and excited states are such that, for $J'' \leq 9$, the $P(J'')$ and $R(J''+3)$ lines overlap within the resolution of the experiment. Observed line positions for the $b^1\Sigma_u^+-X^1\Sigma_g^+(6,0)$ band are listed in table 5 for $^{14}\text{N}_2$, and table 6 for $^{14}\text{N}^{15}\text{N}$.

Term values and spectroscopic parameters were determined from the experimental transition energies using least-squares fitting procedures. The terms of the ground state $X^1\Sigma_g^+$ were represented as

$$F(J'') = B[J''(J''+1)] - D[J''(J''+1)]^2 + H[J''(J''+1)]^3, \quad (1)$$

where B is the rotational constant, and D and H are the centrifugal distortion parameters. The spectroscopic parameters of Trickl *et al.* [24] and Bendtsen [25] were used for the $X^1\Sigma_g^+$ states of $^{14}\text{N}_2$ and $^{14}\text{N}^{15}\text{N}$, respectively. The terms of the excited $^1\Pi_u$ states,

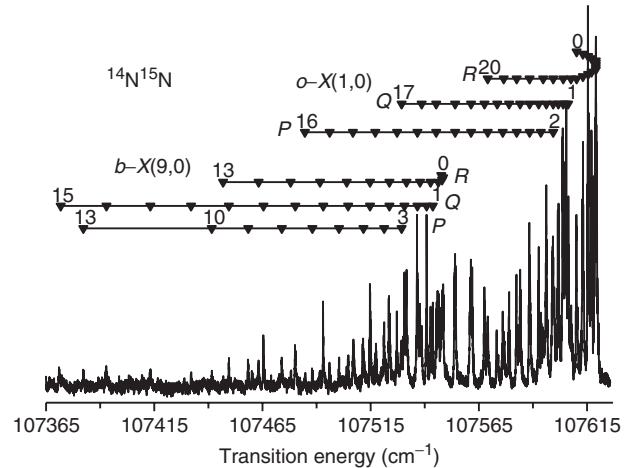


Figure 2. 1 XUV + $1'$ UV ionization spectrum and line assignments for the $b^1\Pi_u-X^1\Sigma_g^+(9,0)$ and $o^1\Pi_u-X^1\Sigma_g^+(1,0)$ bands of $^{14}\text{N}^{15}\text{N}$, recorded using the PDL-based XUV source.

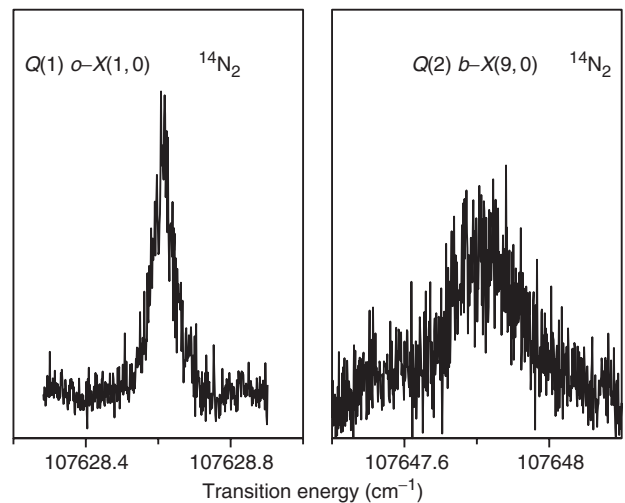


Figure 3. 1 XUV + $1'$ UV ionization spectra of the $Q(2)$ $b^1\Pi_u-X^1\Sigma_g^+(9,0)$ and $Q(1)$ $o^1\Pi_u-X^1\Sigma_g^+(1,0)$ lines of $^{14}\text{N}_2$, recorded using the PDA-based XUV source and showing the different predissociation broadening observed for $b(v=9)$ and $o(v=1)$.

where, for simplicity, we denote the rotational quantum number by J , rather than J' (and the same holds for v and v'), were taken to have the form

$$T_f(J) = \nu_0 + B[J(J+1) - 1] - D[J(J+1) - 1]^2, \quad (2)$$

for the f -parity [26] levels, where ν_0 is the band origin, and

$$T_e(J) = T_f(J) + \Delta T_{ef}(J), \quad (3)$$

for the e -parity levels, where the Λ -doubling is represented by

$$\Delta T_{ef}(J) = q[J(J+1) - 1], \quad (4)$$

Table 1. Observed transition energies (in cm^{-1}) for the $b\ ^1\Pi_u - X\ ^1\Sigma_g^+(9, 0)$ band in $^{14}\text{N}_2$. Deviations from transition energies calculated using the corresponding fitted term values are also shown ($\Delta_{o-c} = \text{obs} - \text{calc}$). Wave numbers given to three decimal places are from narrow-bandwidth PDA spectra, those to two decimal places are from PDL spectra. Wave numbers derived from blended lines are flagged with an asterisk (*) and those from shoulders in the spectra by an s.

J''	$R(J'')$	Δ_{o-c}	$Q(J'')$	Δ_{o-c}	$P(J'')$	Δ_{o-c}
0	107 654.320	-0.075				
1	107 656.14*	0.26	107 650.44	0.02		
2	107 656.01s	-0.26	107 647.840	-0.082	107 642.56	0.10
3	107 656.14*	0.35	107 644.33	-0.01	107 635.85*	-0.14
4	107 635.07*	-0.48	107 640.01*	0.12	107 628.63*	0.19
5					107 619.43*	-0.56
6						
7			107 599.66	0.14		
8	107 611.14*	-0.23	107 588.42*	-0.03	107 567.76	0.04
9			107 575.52	-0.01	107 552.85	0.17
10	107 588.42*	0.05	107 560.96	0.09	107 535.81	0.01
11			107 544.59	0.04	107 517.26	0.07
12	107 558.95	0.01	107 526.84*	0.20	107 497.27*	0.35
13	107 541.93	0.04	107 507.16	0.01	107 475.01	-0.05
14	107 523.12	-0.19	107 486.08	-0.04	107 451.63	0.01
15	107 503.15	-0.06	107 463.49	-0.06	107 427.08*	0.44
16	107 481.50	-0.10	107 439.52	0.06	107 400.09	-0.04
17	107 458.29	-0.20	107 413.80	-0.07	107 372.12	0.01
18	107 433.83	-0.05	107 386.71	-0.06	107 342.58	0.00
19	107 407.77	-0.01	107 358.22	0.04		
20	107 380.25	0.06				
21	107 351.17	0.04				

and q is the Λ -doubling parameter. Rotational energy levels in the $b'(v=6)$ state, of $^1\Sigma_u^+(e)$ symmetry, were represented by

$$T(J) = v_0 + B[J(J+1)] - D[J(J+1)]^2. \quad (5)$$

The $b(v=9)$ and $o(v=1)$ levels in $^{14}\text{N}_2$ give rise to an avoided crossing in the rotational structure between $J=4$ and $J=5$, resulting from a J -independent homogeneous perturbation ($\Delta\Omega=0$, electrostatic) between these valence and Rydberg states. Furthermore, at high J , interaction between the $b'(v=6)$ levels, of $^1\Sigma_u^+$ symmetry, and near-degenerate $o(v=1)$ levels, of $^1\Pi_u$ symmetry, becomes significant. This interaction is heterogeneous ($\Delta\Omega \neq 0$, L-uncoupling) and only involves the e -parity levels of the $o(v=1)$ state. For the e -parity manifold, a full three-state deperturbation analysis was performed for each J value by diagonalizing the matrix

$$\begin{pmatrix} T_{b9} & H_{b9o1} & 0 \\ H_{b9o1} & T_{o1} & H_{o1b'6}\sqrt{J(J+1)} \\ 0 & H_{o1b'6}\sqrt{J(J+1)} & T_{b'6} \end{pmatrix}, \quad (6)$$

where the diagonal elements are the term energies of $b(v=9)$, $o(v=1)$ and $b'(v=6)$, given by equations (2)–(5). The off-diagonal element H_{b9o1} is the two-level homogeneous interaction parameter between the $^1\Pi_u$ states, and $H_{o1b'6}\sqrt{J(J+1)}$ represents the effective heterogeneous interaction matrix element between the $o(v=1)$ and $b'(v=6)$ states. Since the $b'(v=6)$ state has $^1\Sigma_u^+$ symmetry, and therefore only e -parity levels, in the case of the f -parity manifold, equation (6) reduces to a 2×2 matrix.

The resulting deperturbed spectroscopic parameters for $o(v=1)$, $b(v=9)$, and $b'(v=6)$, obtained from a comprehensive least-squares fit for all available spectral lines pertaining to the three band systems, are listed in table 7. In the fitting procedure, the nominal uncertainty in the absolute transition energy for fully resolved lines of reasonable strength was set at 0.1 cm^{-1} . In the case of weak or blended lines, the uncertainty was set at an estimated value in the range $0.15\text{--}0.30\text{ cm}^{-1}$. The lines obtained with the PDA-based laser system have an uncertainty of 0.05 cm^{-1} .

In figure 5, reduced experimental term values are plotted for the $b(v=9)$, $o(v=1)$ and $b'(v=6)$ levels in $^{14}\text{N}_2$, based on the assignments to be discussed below. An avoided crossing between $b(v=9)$ and $o(v=1)$

Table 2. Observed transition energies (in cm^{-1}) for the $o^1\Pi_u - X^1\Sigma_g^+(1, 0)$ band in $^{14}\text{N}_2$. Deviations from transition energies calculated using the corresponding fitted term values are also shown ($\Delta_{o-c} = \text{obs} - \text{calc}$). Wave numbers given to three decimal places are from narrow-bandwidth PDA spectra, those to two decimal places are from PDL spectra. Wave numbers derived from blended lines are flagged with an asterisk (*) and those from shoulders in the spectra by an s.

J''	$R(J'')$	Δ_{o-c}	$Q(J'')$	Δ_{o-c}	$P(J'')$	Δ_{o-c}
0	107 632.73*	0.10				
1	107 634.995	-0.034	107 628.614	-0.039		
2	107 636.456	-0.029	107 627.16	0.08	107 620.81*	0.12
3	107 636.63*	-0.14	107 624.61*	0.05	107 615.20	0.07
4	107 654.66*	-0.13	107 620.81*	-0.06	107 608.58	-0.04
5	107 653.62	0.03	107 635.05*	0.14	107 601.08	0.12
6	107 652.44	0.05	107 629.81	0.04	107 611.00	-0.06
7	107 651.13	0.00	107 624.61*	-0.01	107 601.83	-0.05
8	107 649.73	0.03	107 619.43	0.01	107 592.77	0.05
9	107 647.95*	-0.01	107 614.06s	0.02	107 583.51	-0.01
10	107 645.87	0.02	107 608.51*	0.13	107 574.03*	-0.10
11	107 643.34	0.03	107 602.31	-0.03	107 564.49	0.04
12	107 640.52*	0.20	107 596.01	0.12	107 554.45	0.05
13	107 636.63*	-0.22	107 588.95	-0.03	107 543.94	0.01
14	107 632.73*	-0.14	107 581.62	0.01	107 533.03	0.03
15	107 628.63*	0.22	107 574.03*	0.28	107 521.59	0.00
16	107 623.31	-0.08	107 565.44	0.03	107 509.70	0.01
17	107 617.84	-0.02	107 556.54	-0.02	107 497.24*	-0.05
18	107 611.71	-0.06	107 547.25	0.04	107 484.35	-0.02
19	107 605.09	-0.03	107 537.36	0.01	107 470.88	-0.04
20	107 597.73	-0.11	107 526.84*	-0.14	107 456.92	-0.01
21			107 516.12	0.02	107 442.35	-0.02
22			107 504.68	-0.02	107 427.09*	-0.10
23			107 492.78	-0.01	107 411.26	-0.04
24	107 579.56	0.10	107 480.24	-0.12	107 394.50	0.08
25			107 467.43	0.02	107 375.87	0.33
26			107 453.86	-0.08		

is clearly visible between $J=4$ and 5, with a maximum energy shift of 8.7cm^{-1} at $J=4$, as a result of the homogeneous interaction between the two levels. A second avoided crossing occurs between $J=24$ and 25, associated with the heterogeneous coupling between $o(v=1)$ and $b'(v=6)$, with a maximum shift of 13.5cm^{-1} at $J=25$. In figure 5, only the e -parity levels of both $^1\Pi_u$ states are displayed. For the f -parity components, a similar graph can be constructed, but in this case there is no interaction with the $b'(v=6)$ state. Note that the observed levels in figure 5 are represented by solid symbols, the predicted levels by open symbols. The mixing factors following from the diagonalization procedure using equation (6) are presented in figure 6.

The present line assignments for the $b(v=9) \sim o(v=1)$ complex in $^{14}\text{N}_2$ differ from those in the previous study of Yoshino *et al.* [10]. (The assignments for rotational lines accessing $b(v=9)$ given by Carroll and Collins [3] are erroneous, as already discussed by Yoshino *et al.* [10].) First, we have adopted

a different convention for the labelling of the levels before the crossing ($J=1-4$), assigning the $b(v=9)$ and $o(v=1)$ labels to the levels with the highest mixing factor for the corresponding nominal level. Thus, as shown in figure 5, for J -levels before the crossing, the higher term values belong to $b(v=9)$ and, after the crossing ($J \geq 5$), to $o(v=1)$, while the reverse is true for the lower terms. Yoshino *et al.* [10], in contrast, assigned all the higher and lower term values as $o(v=1)$ and $b(v=9)$, respectively.

Apart from this unimportant difference in nomenclature, we have made some significant reassignments. For $J \geq 5$ in the $b(v=9) \sim o(v=1)$ complex, the assignments of the current and previous [10] studies agree, but, for lines accessing the $J=1-4$ levels of the excited states, the assignments differ. These reassignments were facilitated in the present work by the recording of a number of spectra under differing experimental conditions. Separate PDL-based spectra for relatively low and high rotational temperatures aided

Table 3. Observed transition energies (in cm^{-1}) for the $b^1\Pi_u-X^1\Sigma_g^+(9,0)$ band in $^{14}\text{N}^{15}\text{N}$, from spectra obtained with the PDL-based XUV source. Deviations from transition energies calculated using the corresponding fitted term values are also shown ($\Delta_{o-c} = \text{obs} - \text{calc}$). Wave numbers derived from blended lines are flagged with an asterisk (*) and those from shoulders in the spectra by an s.

J''	$R(J'')$	Δ_{o-c}	$Q(J'')$	Δ_{o-c}	$P(J'')$	Δ_{o-c}
0	107 547.65s	0.01				
1	107 548.47s	-0.12	107 543.70	-0.09		
2	107 548.01s	-0.07	107 540.85	-0.04		
3	107 546.27*	0.14	107 536.60*	0.06	107 529.29*	-0.06
4	107 542.69	-0.03	107 530.62	-0.13	107 521.23	0.08
5	107 537.81	-0.05	107 523.66*	0.16	107 511.66	0.15
6	107 531.56	0.01	107 514.70*	-0.10	107 500.38	-0.03
7	107 523.66*	-0.13	107 504.60	-0.05	107 488.06	0.20
8	107 514.70*	0.13	107 493.09	0.04	107 473.95	0.09
9	107 503.93	0.03	107 480.18	0.19	107 458.43	0.02
10	107 491.60	-0.18	107 465.46	-0.03	107 441.55	0.04
11	107 478.00	-0.20	107 449.48	-0.05		
12	107 463.22	0.06	107 432.00	-0.12		
13	107 446.79	0.12	107 413.18	-0.08	107 382.22	0.12
14			107 392.91	-0.03		
15			107 371.77	0.60		

Table 4. Observed transition energies (in cm^{-1}) for the $o^1\Pi_u-X^1\Sigma_g^+(1,0)$ band in $^{14}\text{N}^{15}\text{N}$, from spectra obtained with the PDL-based XUV source. Deviations from transition energies calculated using the corresponding fitted term values are also shown ($\Delta_{o-c} = \text{obs} - \text{calc}$). Wave numbers derived from blended lines are flagged with an asterisk (*) and those from shoulders in the spectra by an s.

J''	$R(J'')$	Δ_{o-c}	$Q(J'')$	Δ_{o-c}	$P(J'')$	Δ_{o-c}
0	107 610.18*	0.06				
1	107 613.09*	0.14	107 606.26	-0.01		
2	107 615.49*	0.22	107 605.29	0.03	107 599.36*	0.78
3	107 617.07*	-0.02	107 603.99*	0.24	107 593.66	-0.05
4	107 619.03*	0.63	107 601.75	0.02	107 588.45*	0.11
5	107 619.03*	-0.17	107 599.36*	0.15	107 582.49*	0.02
6	107 619.03*	-0.46	107 596.19	0.01	107 576.03*	-0.06
7	107 619.03*	-0.25	107 592.64	-0.01	107 569.11*	-0.09
8	107 619.03*	0.48	107 588.45*	-0.17	107 561.40*	-0.40
9	107 617.07*	-0.25	107 584.06s	-0.02	107 554.02*	0.12
10	107 615.49*	-0.09	107 578.97	-0.08	107 545.27s	-0.22
11	107 613.09*	-0.24	107 573.51	0.00	107 536.60*	0.02
12	107 610.18*	-0.39	107 567.60	0.13	107 527.20	0.04
13	107 607.57*	0.28	107 561.40*	0.46	107 517.15	-0.08
14	107 603.99*	0.49	107 554.02*	0.11	107 506.80	0.00
15	107 599.36*	0.18	107 545.27*	-0.11	107 496.04	0.19
16	107 594.73	0.39	107 538.58s	0.23	107 484.59	0.20
17	107 588.45*	-0.50	107 529.29*	-0.55		
18	107 582.49*	-0.50				
19	107 576.48s	0.07				
20	107 569.11*	0.01				

considerably in the assignment of lines, which may be blended in one or other spectrum, to low or high J'' . Furthermore, the PDA-based measurements were performed with a rather low rotational temperature, so that

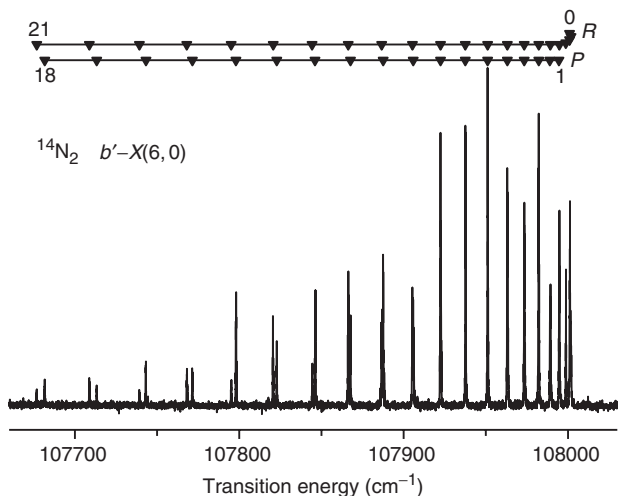


Figure 4. 1 XUV + 1' UV ionization spectrum and line assignments for the $b' \ ^1\Sigma_u^+ - X \ ^1\Sigma_g^+(6, 0)$ band of $^{14}\text{N}_2$, recorded using the PDL-based XUV source.

only lines originating from $J'' = 0-2$ appeared strongly, with possible weak lines from $J'' = 3$ and 4. This conclusion was confirmed independently in measurements of the $b-X(10, 0)$ band in $^{14}\text{N}_2$ [21], recorded under the same experimental conditions. Of course, the most convincing argument for the present line assignments and analysis is the reproducibility of all lines in the fitting procedure using equations (1)–(6). With 163 lines included in the fit, a χ^2 of 93 is found.

The deperturbed rotational constant for $3s\sigma_g o \ ^1\Pi_u(v = 1)$ in table 7, $B = 1.7325 \text{ cm}^{-1}$, is in agreement with expectation for a Rydberg state converging on the $A \ ^2\Pi_u$ ionic state ($B(A, v^+ = 1) = 1.716 \text{ cm}^{-1}$ [27]), with the residual difference occurring because the effects of perturbations by more remote levels are still included in the two-level-deperturbed value. The deperturbed rotational constant for $b(v = 9)$ is significantly lower, $B = 1.2288 \text{ cm}^{-1}$, appropriate for a valence $b \ ^1\Pi_u$ state. The deperturbed D value for $b(v = 9)$ in table 7 is small and negative, comparable to the value $D = -5.5 \times 10^{-6} \text{ cm}^{-1}$ for $^{15}\text{N}_2$ reported in [14]. This negative D value is supported by the observations of Yoshino *et al.* [10], who find some even higher- J P - and Q -branch lines accessing $b(v = 9)$, up to $J = 28$, which exhibit a further gradual shift upward in

Table 5. Observed transition energies (in cm^{-1}) for the $b' \ ^1\Sigma_u^+ - X \ ^1\Sigma_g^+(6, 0)$ band of $^{14}\text{N}_2$, from spectra obtained using the PDL-based XUV source. Deviations from transition energies calculated using the corresponding fitted term values are also shown ($\Delta_{o-c} = \text{obs} - \text{calc}$). Wave numbers derived from blended lines are flagged with an asterisk (*).

J''	$R(J'')$	Δ_{o-c}	$P(J'')$	Δ_{o-c}
0	108 000.93 ^a	0.013		
1	108 001.82	0.08	107 994.49 ^a	-0.045
2	108 000.93 ^a	-0.055	107 988.94 ^a	-0.039
3	107 998.65 ^a	0.004	107 982.23*	0.38
4	107 994.73 ^a	0.012	107 973.35*	0.22
5	107 989.23 ^a	0.033	107 963.09*	0.25
6	107 982.23*	0.15	107 951.11*	0.16
7	107 973.35*	0.00	107 937.50*	0.02
8	107 963.09*	0.09	107 922.44*	0.03
9	107 951.11*	0.08	107 905.84*	0.11
10	107 937.50*	0.08	107 887.58	0.14
11	107 922.44*	0.27	107 867.66	0.14
12	107 905.34*	0.09	107 846.08	0.11
13	107 886.63	-0.04	107 822.81	0.03
14	107 866.31	-0.08	107 797.94	0.01
15	107 844.29	-0.13	107 771.49	0.08
16	107 820.67	-0.06	107 743.23	0.02
17	107 795.15	-0.17	107 713.26	-0.05
18	107 768.04	-0.13	107 681.66	-0.05
19	107 739.27	-0.03		
20	107 708.79	0.08		
21	107 676.76	0.27	107 576.63*	0.08
22			107 538.23*	0.16

^aData taken from PDA-based measurements [21].

energy, by up to several cm^{-1} , for both e - and f -parity components. It is likely that the negative D value for $b(v=9)$ is a result simply of the multilevel perturbation by more distant levels.

The new assignments for the lowest- J levels of $b(v=9)$ and $o(v=1)$ in $^{14}\text{N}_2$ indicate a greater separation in energy than in [10] (especially for $J=1f$ where the separation is larger by 3.4cm^{-1}), resulting in significant differences between the two-level-deperturbed parameters in table 7 and previous values [10]. For example, the fitted homogeneous interaction matrix element, $H_{b9o1} = 9.47\text{cm}^{-1}$, should

be compared with the previously accepted value of 8.10cm^{-1} [10]. It has been pointed out elsewhere [8] that it was the incorrect use of the *deperturbed* experimental $b(v=9)$ and $o(v=1)$ spectroscopic parameters [3, 10] in comparisons with the theoretical results of Stahel *et al.* [5] and Spelsberg and Meyer [6] which led to the large discrepancies, especially in B , for these particular levels. Evidently, the present reassignments will also have some effect in resolving those discrepancies.

The major contribution to the splitting between the e - and f -parity levels of $o(v=1)$ is due to the heterogeneous interaction with the $b'{}^1\Sigma_u^+(v=6)$ state,

Table 6. Observed transition energies (in cm^{-1}) for the $b'{}^1\Sigma_u^+ - X'{}^1\Sigma_g^+(6, 0)$ band of $^{14}\text{N}^{15}\text{N}$, from spectra obtained using the PDL-based XUV source. Deviations from transition energies calculated using the corresponding fitted term values are also shown ($\Delta_{o-c} = \text{obs} - \text{calc}$). Wave numbers derived from blended lines are flagged with an asterisk (*).

J''	$R(J'')$	Δ_{o-c}	$P(J'')$	Δ_{o-c}
0	107 939.54*	-0.03		
1	107 940.32	-0.06	107 933.71*	0.32
2	107 939.54*	-0.14	107 928.30*	0.27
3	107 937.48	0.03	107 921.53*	0.38
4	107 933.71*	0.01	107 913.15*	0.40
5	107 928.46*	0.05	107 903.19*	0.36
6	107 921.53*	-0.05	107 891.68*	0.29
7	107 913.15*	-0.05	107 878.52*	0.11
8	107 903.19*	-0.08	107 863.96*	0.07
9	107 891.68*	-0.08	107 847.76*	-0.07
10	107 878.52*	-0.16	107 830.03*	-0.18
11	107 863.96*	-0.05	107 811.15	0.13
12	107 847.76*	0.03	107 790.35	0.09
13	107 830.03*	0.20	107 767.99	0.08
14	107 810.32	0.02	107 744.19	0.23
15	107 789.15	0.02	107 718.35	-0.04
16	107 766.29	-0.02	107 691.17	-0.03
17	107 741.71	-0.13	107 662.39	0.02
18	107 715.63	-0.08	107 631.92	0.03
19	107 688.06	0.11		
20	107 658.65	-0.01	107 565.96	-0.02
21	107 628.08	0.00		

Table 7. Molecular parameters for the $b'{}^1\Pi_u(v=9)$, $o'{}^1\Pi_u(v=1)$ and the $b'{}^1\Sigma_u^+(v=6)$ states of $^{14}\text{N}_2$ and $^{14}\text{N}^{15}\text{N}$. All values are in cm^{-1} . 1σ statistical uncertainties, resulting from the fit, are shown in parentheses, in units of the last significant figure. Additional systematic uncertainties of order 0.05cm^{-1} apply to the band origins ν_0 .

Species	Level	B	$D \times 10^6$	$q \times 10^3$	ν_0	H_{b9o1}	$H_{o1b'6}$
$^{14}\text{N}_2$	$b'{}^1\Pi_u(v=9)^a$	1.2288(4)	-3.7(8)	0.67(13)	107 647.64(4)	9.47(1)	
$^{14}\text{N}_2$	$o'{}^1\Pi_u(v=1)^a$	1.7325(3)	6.9(5)	-0.81(10)	107 636.43(3)		
$^{14}\text{N}_2$	$b'{}^1\Sigma_u^+(v=6)^a$	1.2005(1)	51.8(3)	-	107 998.51(1)		0.542(4)
$^{14}\text{N}^{15}\text{N}$	$b'{}^1\Pi_u(v=9)$	1.199(1)	7(6)	0 ^b	107 546.44(4)	0 ^b	
$^{14}\text{N}^{15}\text{N}$	$o'{}^1\Pi_u(v=1)^a$	1.6711(6)	2(2)	0 ^b	107 608.45(4)		
$^{14}\text{N}^{15}\text{N}$	$b'{}^1\Sigma_u^+(v=6)^a$	1.1647(4)	56(2)	-	107 937.24(3)		0.67(3)

^aDeperturbed parameters. ^bFixed parameter. No statistically significant value found.

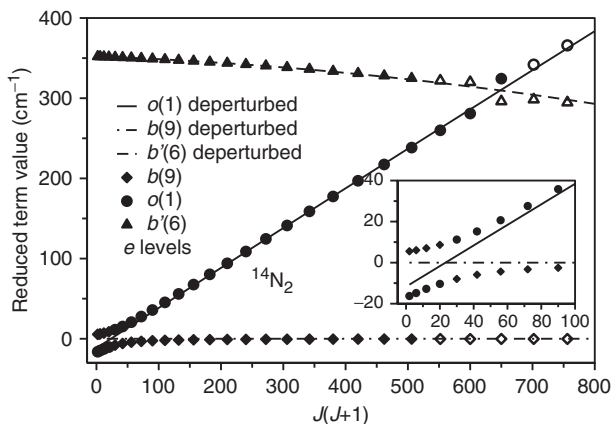


Figure 5. Reduced term values of the $b^1\Pi_u(v=9) \sim o^1\Pi_u(v=1) \sim b'^1\Sigma_u^+(v=6)$ crossings in $^{14}\text{N}_2$ (e -levels only), including the results of an effective three-state deperturbation. The terms are reduced such that the deperturbed $b(v=9)$ levels lie on the zero line. The solid symbols represent measured energy levels, the open symbols predicted levels.

as already discussed by Yoshino *et al.* [10]. Rotational levels in the higher-lying $b'(v=6)$ valence state approach the Rydberg $o(v=1)$ levels from above with increasing J , since $b'(v=6)$ has a smaller B value than $o(v=1)$. This is illustrated in figure 5. For levels with $J \gtrsim 20$, the e -parity components of $o(v=1)$ are pushed down in energy, while the f -parity levels are unaffected. The $R(24)$ line from the $o\text{-X}(1,0)$ band, predicted from the perturbation analysis to lie near $107\,579.2\text{ cm}^{-1}$, was found in the experimental spectrum as a weak satellite, thereby pinpointing the culmination of the heterogeneous interaction. The $R(22)$ line of $o\text{-X}(1,0)$ is predicted to coincide with the $P(7)$ line of $b\text{-X}(9,0)$, while $R(21)$ would coincide with $Q(13)$ of $o\text{-X}(1,0)$. $R(23)$ is probably too weak to be observed under our experimental conditions. Unfortunately, lines accessing the $b'(v=6)$ perturbation partner could only be followed up to $R(21)$ and $P(22)$, below the crossing point. We note that the $P(26)$ line in $o\text{-X}(1,0)$, reported by Yoshino *et al.* [10], does not match the present analysis and is reassigned as the $Q(19)$ line of $b\text{-X}(9,0)$. Despite the somewhat incomplete nature of the experimental data defining the $b'(v=6) \sim o(v=1, e)$ crossing, it has been possible to determine a heterogeneous interaction matrix element $H_{o1b'6} = 0.542\text{ cm}^{-1}$, which is of a similar order to those found by Yoshino *et al.* [10] for crossings involving other vibrational levels of the same states: $H_{o0b'3} = 0.29\text{ cm}^{-1}$, $H_{o3b'11} = 0.44\text{ cm}^{-1}$, and $H_{o4b'14} = 0.60\text{ cm}^{-1}$. The three-level-deperturbed Λ -doubling parameters q given in table 7 for the $o(v=1)$ and $b(v=9)$ states, which are negative and positive, respectively, agree in sign with those

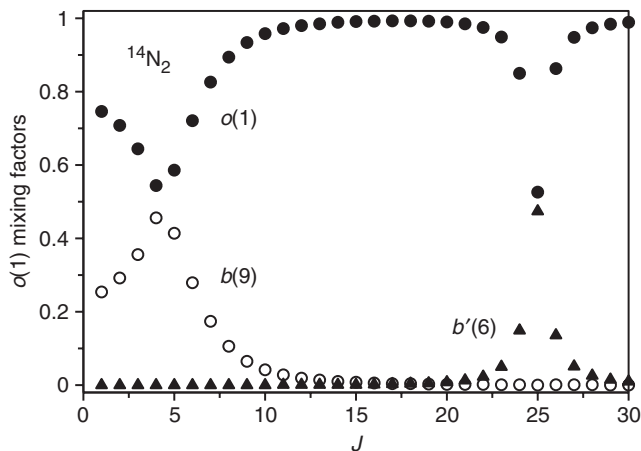


Figure 6. Calculated $o(v=1)$ mixing factors for the $o^1\Pi_u(v=1)$, $b^1\Pi_u(v=9)$, and $b'^1\Sigma_u^+(v=6)$ levels of $^{14}\text{N}_2$. Plotted is the absolute square $|c_i|^2$ of the coefficients c_i representing the projection of the wave function $\Psi_{o(1)}$ on a basis of unperturbed wave functions ($\phi_{o(1)}, \phi_{b(9)}, \phi_{b'(6)}$). The data pertain to the e -parity component only.

determined for $^{15}\text{N}_2$ by Sprengers *et al.* [14]. These residual Λ -doublings are likely caused, directly or indirectly, by heterogeneous interactions between $o(v=1)$ and other more remote levels of the $b'^1\Sigma_u^+$ perturber.

In $^{14}\text{N}^{15}\text{N}$, the $b(v=9)$ level shifts further down in energy than the $o(v=1)$ level following isotopic substitution. Therefore, the order of the two states is reversed and the lower-lying $b(v=9)$ level, with the smaller B value, does not cross the higher-lying $o(v=1)$. The same is true for $^{15}\text{N}_2$ [14]. As a consequence, in the fitting procedure for $^{14}\text{N}^{15}\text{N}$ it was not possible to determine a meaningful homogeneous interaction parameter H_{b9o1} , which was therefore set to zero. Furthermore, due to the inferior signal-to-noise ratio for the $^{14}\text{N}^{15}\text{N}$ spectra, the highest- J levels could not be observed, making it difficult to define the inherent Λ -doubling parameters for both the $b(v=9)$ and $o(v=1)$ states. Accordingly, these parameters were also set to zero, as including them in the fit of 132 lines did not improve the χ^2 value of 93. Although it was not possible experimentally to follow the $b'(v=6)$ and $o(v=1)$ levels of $^{14}\text{N}^{15}\text{N}$ to high enough J values to define the expected avoided-crossing region, a significant reduction in χ^2 was obtained by including the corresponding heterogeneous interaction parameter in the fitting procedure, principally due to its ability to reproduce the $o(v=1)$ -state Λ -doubling observed experimentally. The fitted spectroscopic parameters for $^{14}\text{N}^{15}\text{N}$ are given in table 7. In the case of the heterogeneous interaction between $b'(v=6)$ and $o(v=1, e)$, the interaction

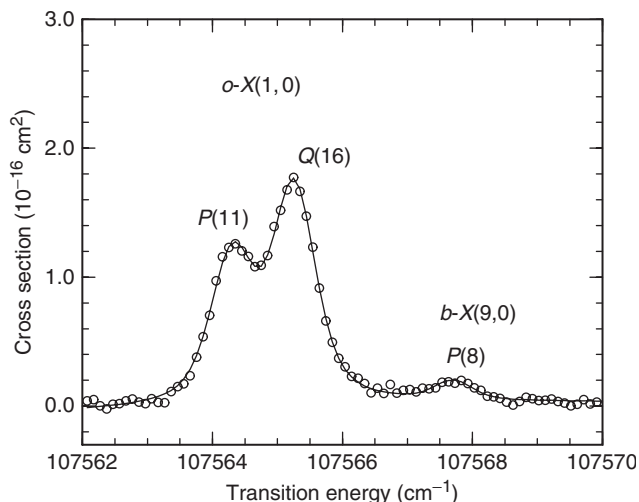


Figure 7. Experimental room-temperature photoabsorption cross section for a region of the overlapping $b\text{-X}(9,0)$ and $o\text{-X}(1,0)$ bands of $^{14}\text{N}_2$ (open circles), together with the fitted cross section (solid curve). The $P(8)$ line from the $b\text{-X}(9,0)$ band, probing $J=7$, is anomalously weak (see text).

parameter, $H_{o1b/6} = 0.67\text{ cm}^{-1}$, is of the same order as the value obtained for $^{14}\text{N}_2$. A crossing of the $b'(v=6)$ and $o(v=1, e)$ levels between $J=24$ and 25 is predicted by the fit, with a maximum shift of $\sim 13\text{ cm}^{-1}$ at $J=24$. The B values given in table 7 are slightly lower in the mixed isotopomer due to the greater reduced mass.

3.2. Oscillator strengths

The Photon Factory experimental photoabsorption cross sections were analysed using a least-squares fitting procedure in which each line was represented by a Voigt profile and account was taken of the effects of the finite experimental resolution. The line oscillator strength and the Lorentzian width component, corresponding to the predissociation linewidth, for each Voigt line were parameters of the fit, while the Gaussian width component was fixed at the room-temperature Doppler width of 0.24 cm^{-1} FWHM. The instrumental function was also defined by a Voigt profile, with Gaussian and Lorentzian width components of 0.60 and 0.20 cm^{-1} FWHM, respectively, determined by analysing scans over the almost pure Doppler lines from the $c_4^1\Sigma_u^+ - X^1\Sigma_g^+(0,0)$ band [28]. The Voigt-model cross section was convolved, in the transmission domain, with the instrumental function, and compared iteratively with the experimental cross section. In the case of weak lines, it was not possible to independently determine the predissociation linewidths, which were fixed at realistic values interpolated from other known widths (see section 3.3), but, in any case, the fitted oscillator strengths were not very sensitive to these

Table 8. Experimental (perturbed) band oscillator strengths f for the $b\text{-X}(9,0)$ and $o\text{-X}(1,0)$ transitions of $^{14}\text{N}_2$. Values flagged with an asterisk (*) are derived only from blended lines. 1σ statistical uncertainties are shown in parentheses, in units of the last significant figure. Additional systematic uncertainties of $\approx 10\%$ are applicable.

J	$f_{b\text{-X}(9,0)}$	$f_{o\text{-X}(1,0)}$
1	0.0154(8)*	0.0029(6)*
2	0.0147(3)*	0.0022(2)*
3	0.0160(3)	0.0017(3)*
4	0.0164(2)*	0.0006(2)*
5	0.0005(2)*	0.0181(3)
6		0.0170(2)
7	0.0007(1)	0.0178(3)
8	0.0014(1)	0.0172(2)
9	0.0022(2)	0.0161(3)
10	0.0031(1)	0.0149(2)
11	0.0030(1)*	0.0145(2)
12	0.0036(2)	0.0139(3)
13	0.0037(1)	0.0138(2)
14	0.0037(1)	0.0143(2)
15	0.0039(2)	0.0132(2)
16	0.0043(1)	0.0135(2)*
17	0.0039(3)	0.0120(4)
18	0.0042(2)	0.0121(3)
19	0.0041(3)	0.0122(5)
20	0.0042(5)	0.0137(5)*

adopted linewidths. In the case of overlapping lines, generally the line-strength ratios were fixed at the values expected from Hönl–London- and Boltzmann-factor considerations and an average oscillator strength determined. The fitting procedure is illustrated in figure 7. In this example, it was possible to determine independent oscillator strengths for the stronger, partially overlapped $P(11)$ and $Q(16)$ lines from the $o\text{-X}(1,0)$ band, but only a common predissociation linewidth. For the very weak $P(8)$ line from the $b\text{-X}(9,0)$ band, however, only the oscillator strength could be determined.

The fitted line oscillator strengths were converted into band oscillator strengths by dividing by appropriately normalized $^1\Pi\text{-}^1\Sigma$ Hönl–London factors and fractional initial-state populations, the latter determined from $T=295\text{ K}$ Boltzmann factors based on the N_2 ground-state term values, and taking into account the 2:1 rotational intensity alternation caused by nuclear-spin effects. No significant systematic differences were found between the P -, Q -, or R -branch band oscillator strengths, for either the $b\text{-X}(9,0)$ or $o\text{-X}(1,0)$ transitions, over the range of rotation studied, $J \leq 20$. The overall results, summarized in table 8 and

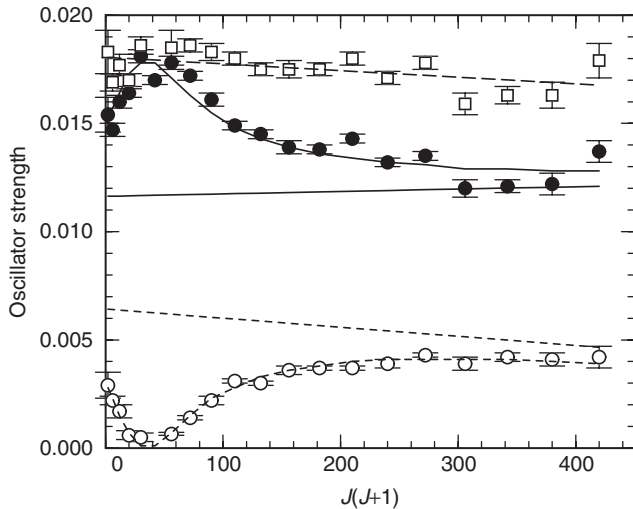


Figure 8. Rotational $J(=J)$ dependence of band oscillator strengths in the mixed $b\text{-X}(9,0)$ and $o\text{-X}(1,0)$ transitions of $^{14}\text{N}_2$, demonstrating a strong quantum-interference effect near $J=6$, together with the results of a deperturbation analysis (see text). Solid circles: experimental (perturbed) oscillator strengths for transitions to the higher-energy levels for a given J . Open circles: experimental oscillator strengths for transitions to the lower-energy levels. Solid line: deperturbed oscillator strength for the $o\text{-X}(1,0)$ transition. Dashed line: deperturbed oscillator strength for the $b\text{-X}(9,0)$ transition. Solid curve: calculated perturbed oscillator strength for the higher levels. Dashed curve: calculated perturbed oscillator strength for the lower levels. Open squares: sum of experimental oscillator strengths for a given J . Long-dashed line: sum of calculated perturbed (or deperturbed) oscillator strengths.

illustrated in figure 8 (circles), represent weighted means over each available branch.

Inspection of figure 8 reveals an interesting effect: transitions to the higher-energy levels ($b(v=9)$ for $J \leq 4$, $o(v=1)$ for $J \geq 5$; solid circles) peak in strength near $J=6$, while those to the lower-energy levels ($o(v=1)$ for $J \leq 4$, $b(v=9)$ for $J \geq 5$; open circles) decrease rapidly in intensity in the same region, with transitions to $J=6$ too weak to be observed. This is a classic example of a two-level quantum-mechanical interference effect, in the case where transitions to both levels, of like symmetry, carry an oscillator strength, as discussed in detail by Lefebvre-Brion and Field [26]. The perturbed vibronic oscillator strengths for transitions from a common level 0 to the upper (+) and lower (−) levels of the interacting pair, respectively, are given by [26]:

$$\begin{aligned} f_{+0} &= c^2 f_{10} + (1 - c^2) f_{20} \pm 2c \sqrt{(1 - c^2) f_{10} f_{20}}, \\ f_{-0} &= (1 - c^2) f_{10} + c^2 f_{20} \mp 2c \sqrt{(1 - c^2) f_{10} f_{20}}, \end{aligned} \quad (7)$$

where f_{10} and f_{20} are the vibronic oscillator strengths for transitions to the unperturbed levels, 1 and 2, and $c > 0$ is the mixing coefficient corresponding to the presence of the unperturbed level 1 in the perturbed upper-level wave function. The sense of the interference effect, corresponding to the signs of the right-hand terms in equation (7), depends on the sign of $\mu_{10}\mu_{20}H_{12}$, where the μ_{i0} are vibronic transition moments ($f_{i0} \propto \mu_{i0}^2$) and H_{12} is the coupling matrix element [26]. The present case, where the higher-energy transitions are enhanced in strength by the interference effect, corresponds to $\mu_{bX(9,0)}\mu_{oX(1,0)}H_{b9o1} > 0$.

Using the f -level mixing coefficients determined as part of the energy-level deperturbation procedure described in section 3.1, together with the experimental (perturbed) oscillator strengths from table 8, we have successfully deperturbed the oscillator strengths through the application of equation (7). In contrast to the perturbed case, the deperturbed oscillator strengths display only slight J dependencies, yielding the following fits: $f_{bX(9,0)} = 0.0064(2) - 4.2(9) \times 10^{-6}J(J+1)$ (dashed line in figure 8), $f_{oX(1,0)} = 0.0116(3) + 1.1(11) \times 10^{-6}J(J+1)$ (solid line in figure 8). Back-generating the perturbed oscillator strengths from these fits yields the results shown in figure 8 for the upper and lower levels (solid curve, dashed curve, respectively), which are seen to be in excellent agreement with the measurements. Furthermore, the summed deperturbed (or perturbed) fitted oscillator strengths (long-dashed line in figure 8) are in good agreement with the summed experimental values (open squares), neither exhibiting any strong J dependence, as would be expected in the case of the simple two-level interaction described by equation (8). While the $b(v=9) \sim o(v=1)$ crossing occurs between $J=4\text{--}5$, the intensity minimum for transitions to the lower of the perturbed levels appears to occur just below $J=6$. This difference is a consequence of the deperturbed $f_{oX(1,0)}$ significantly exceeding $f_{bX(9,0)}$. From equation (7), only in the specific case $f_{10} = f_{20}$ will an intensity zero occur at the level crossing ($c = 1/\sqrt{2}$).

These results confirm that the $b(v=9) \sim o(v=1)$ level crossing in $^{14}\text{N}_2$ produces a simple two-level quantum-mechanical interference effect in the corresponding perturbed oscillator strengths for transitions from the ground state, yielding a virtually complete destructive interference for transitions to the lower level with $J=6$ (principally of $b(v=9)$ character). As will be seen in section 3.3, the situation for the corresponding predissociation linewidths is somewhat more complicated. Finally, we note that an ostensibly similar deep minimum in oscillator strength has been reported in $^{14}\text{N}_2$ for transitions to $b(v=8)$ near $J=12$ [9]. This latter case is distinguished, however, by *no level crossing*

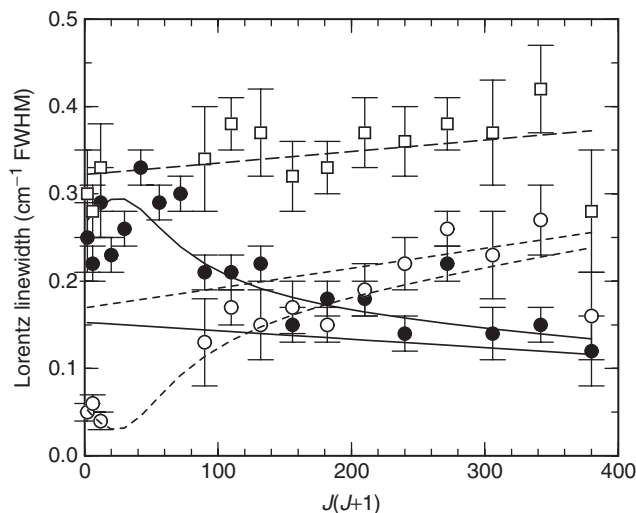


Figure 9. Rotational dependence of predissociation linewidths for the mixed $b(v=9)$ and $o(v=1)$ states of $^{14}\text{N}_2$, together with the results of a deperturbation analysis (see text). Solid circles: experimental (perturbed) widths for the higher-energy levels. Open circles: experimental widths for the lower-energy levels. Solid line: deperturbed $o(v=1)$ widths. Dashed line: deperturbed $b(v=9)$ widths. Solid curve: calculated perturbed widths for the higher levels. Dashed curve: calculated perturbed widths for the lower levels. Open squares: sum of experimental widths for a given J . Long-dashed line: sum of calculated perturbed (or deperturbed) widths.

being involved, the destructive interference effect being a multilevel phenomenon.

3.3. Predissociation linewidths

Lorentzian linewidth components for individual rotational levels of $b(v=9)$ and $o(v=1)$ in $^{14}\text{N}_2$, dominated by the contribution of predissociation over radiation, were determined from both the PDA laser-based ionization spectra and the Photon Factory photoabsorption spectra. Of course, the PDA-based system was to be preferred for the measurement of linewidths because of its superior resolution and Doppler-reduced character, but, in practice, these advantages applied only at low J in the cold spectra, since the room-temperature background gas contribution dominated the jet contribution for higher J . On the other hand, the high signal-to-noise ratio of the photoabsorption spectra made them suitable for the determination of Lorentzian linewidth components with $\Gamma \gtrsim 0.15 \text{ cm}^{-1}$ FWHM, albeit with significant uncertainty, even with an experimental resolution of only $\sim 0.7 \text{ cm}^{-1}$ FWHM. Predissociation linewidths, determined from the PDA-based spectra by deconvolving the instrument width from the observed widths as explained in [29], and from the photoabsorption spectra,

Table 9. Experimental (perturbed) predissociation linewidths Γ (in cm^{-1} FWHM) for the $b^1\Pi_u(v=9, J)$ and $o^1\Pi_u(v=1, J)$ levels of $^{14}\text{N}_2$. Values flagged with an asterisk (*) are derived only from blended lines. 1σ statistical uncertainties are shown in parentheses, in units of the last significant figure. Additional systematic uncertainties of $\approx 25\%$ are applicable to the non-PDA measurements.

J	$\Gamma_{b(v=9)}$	$\Gamma_{o(v=1)}$
1	0.25(4) ^a	0.05(1) ^a
2	0.22(2) ^a	0.06(1) ^a
3	0.29(4)	0.04(1) ^a
4	0.23(2)*	
5		0.26(2)
6		0.33(2)
7		0.29(2)
8		0.30(2)
9	0.13(5)	0.21(2)
10	0.17(2)	0.21(2)
11	0.15(4)*	0.22(2)
12	0.17(3)	0.15(2)
13	0.15(2)	0.18(2)
14	0.19(3)	0.18(2)
15	0.22(3)	0.14(2)
16	0.26(2)	0.22(2)*
17	0.23(5)	0.14(3)
18	0.27(4)	0.15(2)
19	0.16(5)	0.12(4)

^aPDA measurements.

simultaneously with the oscillator strengths as described in section 3.2, are summarized in table 9 and figure 9. Since no significant systematic e/f parity dependence was found for either the $b(v=9)$ or $o(v=1)$ level widths, the values presented represent weighted means over determinations from each available branch.

The PDA-based system was used only to determine level widths for $b(v=9, J=1-2)$ and $o(v=1, J=1-3)$, i.e. restricted to J -levels below the crossing. The average predissociation linewidths in this region, $\Gamma_{b(v=9)} \approx 0.24 \text{ cm}^{-1}$ FWHM and $\Gamma_{o(v=1)} \approx 0.05 \text{ cm}^{-1}$ FWHM, differ substantially (see also figure 3). They are equivalent to lifetimes $\tau = 1/2\pi\Gamma$ of 23(5) ps and 105(30) ps, for $b(v=9)$ and $o(v=1)$, respectively, which agree with previous time-domain pump–probe lifetime measurements [22]. In [22], the rotational structure of the $b(v=9) \sim o(v=1)$ complex was not resolved and the lifetimes observed, determined mainly by predissociation, varied from <50 ps to 110 ps. From the present study, it can be deduced unambiguously that the <50 -ps component arose from $b(v=9)$ and the 110-ps component from $o(v=1)$. The predissociation

lifetimes of these two levels in $^{15}\text{N}_2$ have been determined with the same frequency-mixing PDA-based XUV source in [21]. For $b(v=9)$ in $^{15}\text{N}_2$, an f -parity lifetime of 46(7)ps was found, a factor of 2 higher than in $^{14}\text{N}_2$. The lifetime of $o(v=1)$ is also isotope dependent: a lifetime of 27(6)ps was obtained for this level in $^{15}\text{N}_2$ [21], a factor of 4 lower than in $^{14}\text{N}_2$. All data pertaining to $^{14}\text{N}^{15}\text{N}$ were obtained here with the PDL-based XUV source and do not, therefore, yield reliable information on the excited-state lifetimes.

While it is not possible unambiguously to detect any systematic J dependence in the PDA linewidths, when taken together with the Photon Factory results, it is evident from figure 9, despite considerable uncertainty in the data, that the width of the lower-energy levels (open circles) increases substantially as J increases, while the width of the higher-energy levels (solid circles) decreases overall, exhibiting a maximum near $J=6$. Because of line overlap and the weakness of the corresponding transitions (see figure 8), we have been unable to determine widths for the lower-energy levels with $J=4-8$.

In the case of a simple, two-level interaction where both (unperturbed) levels predissociate *via the same route*, i.e. *coherently*, a quantum-interference effect in the widths would be expected, analogous to that observed for the corresponding oscillator strengths. In this case, the width interference is described by expressions similar to equation (7), with the widths Γ replacing the oscillator strengths f [26]. The width maximum observed near $J=6$ for the upper-energy levels in figure 9 supports the notion of a width quantum-interference effect associated with the $b(v=9) \sim o(v=1)$ level crossing. However, despite an inability to fully monitor the lower-energy widths in this region, there is no rapid decrease in the $J=1-3$ level widths indicated by the PDA results, contrary to the case of the oscillator strengths in figure 8. Thus, while there may be a minimum in the lower-energy widths near the crossing region, that minimum is unlikely to be as deep as the effectively zero value exhibited by the corresponding oscillator strengths, and required for a coherent two-level interaction.

An initial attempt to deperturb the level widths in figure 9, using the width analogue of equation (7), together with the same mixing coefficients used for the oscillator-strength deperturbation, failed because such a totally destructive quantum interference for the lower-energy levels was incompatible with the experimental widths. Thus, the implied non-zero width minimum for the lower-energy levels suggests that an additional, *incoherent*, and thus additive, width component is

applicable to these levels. If a J -independent value of $\sim 0.03 \text{ cm}^{-1}$ FWHM is assumed for this component, together with coherent two-level interference for the remainder, then the realistic deperturbation shown in figure 9 results, yielding the following fits: $\Gamma_{b(v=9)} = 0.17(2) + 2.3(8) \times 10^{-4} J(J+1) \text{ cm}^{-1}$ FWHM (dashed line in figure 9), including the incoherent component, and $\Gamma_{o(v=1)} = 0.15(1) - 1.0(4) \times 10^{-4} J(J+1) \text{ cm}^{-1}$ FWHM (solid line in figure 9). Back-generating the perturbed widths from these fits yields the results shown in figure 9 for the upper and lower levels (solid curve, dashed curve, respectively), which, as for the oscillator strengths, are in excellent agreement with the experimental measurements. The summed deperturbed (or perturbed) fitted widths (long-dashed line in figure 9) are in good agreement with the summed experimental values (open squares), neither exhibiting any strong J dependence. It is of interest that the two-level-deperturbed low- J predissociation lifetimes implied by the above linewidth analysis, 31(4)ps and 35(3)ps, for $b(v=9)$ and $o(v=1)$, respectively, are in much better agreement with the $^{15}\text{N}_2$ experimental lifetimes, 46(7)ps and 27(6)ps [21], than are the perturbed lifetimes. This indicates that the bulk of the large experimental isotope effect is caused simply by the interference effect associated with the two-level crossing in $^{14}\text{N}_2$.

According to Lewis *et al.* [8], the lowest $^1\Pi_u$ states of N_2 are predissociated, ultimately, by the $C'^3\Pi_u$ state, which correlates with the $^4\text{S} + ^2\text{D}$ dissociation limit at $\sim 97\,940 \text{ cm}^{-1}$. On this basis, the fact that the higher-energy levels are enhanced in width by the interference effect indicates that the matrix-element product $H_{b9C'}H_{o1C'}H_{b9o1} > 0$, where the bound-free vibronic elements relate to the unperturbed widths ($\Gamma_i \propto H_{iC'}^2$). The question remains as to the source of the incoherent contribution to the $b(v=9)$ widths. We propose here that it is the interaction with a repulsive state, namely the second valence state of $^3\Sigma_u^+$ symmetry, labelled $3^3\Sigma_u^+$ by Minaev *et al.* [30], which provides the additional incoherent predissociation of the $b^1\Pi_u$ state. The potential-energy curve for the $3^3\Sigma_u^+$ state, which also correlates with the $^4\text{S} + ^2\text{D}$ limit, crosses that of the $b^1\Pi_u$ state on its outer limb, near $R = 1.75 \text{ \AA}$, at an energy of $\sim 107\,300 \text{ cm}^{-1}$ [31]. Thus, it is energetically possible for the $3^3\Sigma_u^+$ state to predissociate $b^1\Pi_u(v=9)$, which lies near $107\,640 \text{ cm}^{-1}$ (see table 7). Furthermore, the spin-orbit coupling ($\Delta\Omega = 0$) between the $b^1\Pi_u$ and $3^3\Sigma_u^+$ states has been estimated *ab initio* to be on the order of 7 cm^{-1} [32], making this the likely incoherent predissociation mechanism supplying the additional $\sim 0.03 \text{ cm}^{-1}$ FWHM width to $b(v=9)$.

4. Summary and conclusions

Two distinct high-resolution experimental techniques, 1 XUV + 1' UV laser-based ionization spectroscopy and synchrotron-based XUV photoabsorption spectroscopy, have been used to study the $o^1\Pi_u(v=1) \sim b^1\Pi_u(v=9)$ Rydberg–valence complex of $^{14}\text{N}_2$, providing new and detailed information on the perturbed rotational structures, oscillator strengths, and predissociation linewidths. Ionization spectra probing the $b^1\Sigma_u^+(v=6)$ state of $^{14}\text{N}_2$, which crosses $o^1\Pi_u(v=1)$ between $J=24$ and $J=25$, and the $o^1\Pi_u(v=1)$, $b^1\Pi_u(v=9)$, and $b^1\Sigma_u^+(v=6)$ states of $^{14}\text{N}^{15}\text{N}$, have also been recorded. In the case of $^{14}\text{N}_2$, rotational and deperturbation analyses correct previous misassignments for the low- J levels of $o(v=1)$ and $b(v=9)$. In addition, a two-level quantum-mechanical interference effect has been found between the $o\text{-X}(1,0)$ and $b\text{-X}(9,0)$ transition amplitudes which is totally destructive for the lower-energy levels just above the level crossing, making it impossible to observe transitions to $b(v=9, J=6)$. A similar interference effect is found to affect the $o(v=1)$ and $b(v=9)$ predissociation linewidths, but, in this case, a small non-interfering component of the $b(v=9)$ linewidth is indicated, attributed to an additional spin–orbit predissociation by the repulsive $3^3\Sigma_u^+$ state. The experimental linewidths, together with the corresponding interference effect, will provide a challenging test for coupled-channel models of the predissociation dynamics for the $^1\Pi_u$ states of N_2 .

Acknowledgements

The authors gratefully acknowledge the support provided for this research by the following bodies: the Molecular Atmospheric Physics (MAP) Program of the Netherlands Foundation for Fundamental Research on Matter (FOM); the Australian Research Council's Discovery Program (project number DP0558962); and NASA (grant NNG05GA03G). The assistance of the staff of the Photon Factory is also acknowledged.

References

- [1] H. Lefebvre-Brion, *Can. J. Phys.* **47**, 541 (1969).
- [2] K. Dressler, *Can. J. Phys.* **47**, 547 (1969).
- [3] P. K. Carroll and C. P. Collins, *Can. J. Phys.* **47**, 563 (1969).
- [4] M. Ogawa, Y. Tanaka, and A. S. Jursa, *Can. J. Phys.* **42**, 1716 (1964).
- [5] D. Stahel, M. Leoni, and K. Dressler, *J. Chem. Phys.* **79**, 2541 (1983).
- [6] D. Spelsberg and W. Meyer, *J. Chem. Phys.* **115**, 6438 (2001).
- [7] S. A. Edwards, W.-Ü L. Tchang-Brillet, J.-Y. Roncin, F. Launay, and F. Rostas, *Planet. Space Sci.* **43**, 67 (1995).
- [8] B. R. Lewis, S. T. Gibson, W. Zhang, H. Lefebvre-Brion, and J.-M. Robbe, *J. Chem. Phys.* **122**, 144302 (2005).
- [9] V. E. Haverd, B. R. Lewis, S. T. Gibson, and G. Stark, *J. Chem. Phys.* **123**, 214304 (2005).
- [10] K. Yoshino, Y. Tanaka, P. K. Carroll, and P. Mitchell, *J. Molec. Spectrosc.* **54**, 87 (1975).
- [11] K. Yoshino and D. E. Freeman, *Can. J. Phys.* **62**, 1478 (1984).
- [12] K. Yoshino and Y. Tanaka, *J. Molec. Spectrosc.* **66**, 219 (1977).
- [13] P. F. Levelt and W. Ubachs, *Chem. Phys.* **163**, 263 (1992).
- [14] J. P. Sprengers, W. Ubachs, K. G. H. Baldwin, B. R. Lewis, and W.-Ü L. Tchang-Brillet, *J. Chem. Phys.* **119**, 3160 (2003).
- [15] K. P. Huber and Ch. Jungen, *J. Chem. Phys.* **92**, 850 (1990).
- [16] K. P. Huber, Ch. Jungen, K. Yoshino, K. Ito, and G. Stark, *J. Chem. Phys.* **100**, 7957 (1994).
- [17] Ch. Jungen, K. P. Huber, M. Jungen, and G. Stark, *J. Chem. Phys.* **118**, 4517 (2003).
- [18] W. Ubachs, K. S. E. Eikema, and W. Hogervorst, *Appl. Phys. B* **57**, 411 (1993).
- [19] S. Gerstenkorn and P. Luc, *Atlas du spectra d'absorption de la molecule d'iode*, Laboratoire Aimé Cotton, CNRS II, 91405 Orsay (France), 15 600 cm^{-1} –17 600 cm^{-1} (1977).
- [20] J. Philip, J. P. Sprengers, P. Cacciani, C. A. de Lange, and W. Ubachs, *Appl. Phys. B* **78**, 737 (2004).
- [21] J. P. Sprengers and W. Ubachs, *J. Molec. Spectrosc.* **235**, 176 (2006).
- [22] J. P. Sprengers, A. Johansson, A. L'Huillier, C.-G. Wahlström, B. R. Lewis, and W. Ubachs, *Chem. Phys. Lett.* **389**, 348 (2004).
- [23] G. Stark, K. P. Huber, K. Yoshino, P. L. Smith, and K. Ito, *J. Chem. Phys.* **123**, 214303 (2005).
- [24] T. Trickl, D. Proch, and K. L. Kompa, *J. Molec. Spectrosc.* **171**, 374 (1995).
- [25] J. Bendtsen, *J. Raman Spectrosc.* **32**, 989 (2001).
- [26] H. Lefebvre-Brion and R. W. Field, *The Spectra and Dynamics of Diatomic Molecules* (Elsevier, Amsterdam, 2004), pp. 144, 378, 540.
- [27] K. P. Huber and G. Herzberg, *Molecular Spectra and Molecular Structure IV. Constants of Diatomic Molecules* (Van Nostrand, New York, 1979), p. 426.
- [28] G. Stark, K. P. Huber, K. Yoshino, M. C. Chan, T. Matsui, P. L. Smith, and K. Ito, *Astrophys. J.* **531**, 321 (2000).
- [29] J. P. Sprengers, W. Ubachs, and K. G. H. Baldwin, *J. Chem. Phys.* **122**, 144301 (2005).
- [30] B. Minaev, P. Norman, D. Jonsson, and H. Ågren, *Chem. Phys.* **190**, 11 (1995).
- [31] C. E. Dateo, personal communication.
- [32] B. F. Minaev, personal communication.